Desalination and Water Treatment
www.deswater.com
doi: 10.5004/dwt.2021.27666

236 (2021) 1–15
October

Numerical investigation on steam flow and resistance to thermodynamic losses inside the full-scale low-temperature multi-effect desalination evaporator

Yun She[a], Fucheng Chang[a], Wen Chan[a], Yousen Zhang[b], Huixiong Li[a,*]

[a]*State Key Laboratory of Multiphase Flow in Power Engineering, Xi'an Jiaotong University, Xi'an 710049, China, Tel. +86-130-2289-1256; emails: huixiong@mail.xjtu.edu.cn (H. Li), she.y.ab@m.titech.ac.jp (Y. She), 1454504477@qq.com (F. Chang), chanwen@stu.xjtu.edu.cn (W. Chan)*
[b]*Shenhua Guohua (Beijing) Electric Power Research Institute Co., Ltd., Beijing 100025, China, email: zhangyousen@126.com*

Received 31 March 2021; Accepted 22 July 2021

ABSTRACT

3D numerical simulation on the steam velocity field and flow resistance configuration in the full-scale low-temperature multi-effect desalination (LT-MED) evaporator were conducted and analyzed. The complicated two-phase water-vapor flow through the tube bundle was modeled using the single-phase vapor flow through the porous media (PM) model, which could simplify the effect of anfractuous geometry of the flow path and interactions between the two phases in the tube bundle. A PM model has been validated by additional experimental results. 3D numerical results were justified between the literature and real LT-MED plants. The numerical results suggest that the steam velocity in the tube bundle ranges from 1 to 12 m/s and presents different variation trends along the direction of the tube row, tube column, and tube length. In the axial channel, steam velocity first exhibits a rising tendency up to maximum of 50 m/s close to the outlet and then greatly decreases beyond the outlet. The components of steam flow resistance comprise tube bundle, demister, steam channel, and tube-side condensation resistances. The largest flow resistance is contributed by the axial steam channel, accounting for 57.6% proportion. The small steam flow resistance with a total of 381.6 Pa in the first-effect evaporator causes a significant reduction in the effective heat transfer temperature difference by a proportion of 12.2%. This study endeavors to find a new possibility of numerical simulation for the entire LT-MED evaporator, which could provide a good reference to engineering-optimized design and modeling of the LT-MED running condition.

Keywords: Thermal desalination; Flow resistance; Thermodynamic losses; Low-temperature multi-effect desalination; Numerical simulation

1. Introduction

The natural resource of freshwater plays a vital role in economic development and population growth. However, the shortage of potable water resources continues to persist in many regions or countries [1], with 2–7 billion people facing fresh water scarcity [2,3]. The development of desalination technologies is the most effective way to meet the increasing freshwater requirements worldwide. In recent years, desalination markets are dominated by the most popular membrane-based (reverse osmosis theory) and thermal-based technologies (evaporation theory) [3,4]. Among the thermal-based desalination technologies, the low-temperature multi-effect desalination (LT-MED) is the most potential method that utilizes the horizontal-tube falling film evaporator (HTFFE) owing to its various advantages, such as low heat transfer temperature difference (from 1.5°C to 4°C only) [5], low energy consumption, high heat transfer coefficient [6], low manufacturing cost, corrosion resistance [7], easy coupling with thermal [8], nuclear [9], or solar power plants [10]. In contrast with the traditional heat exchanger, the HTFFE is operated in the vacuum working

* Corresponding author.

condition ranging from 21.8 kPa in the first-effect evaporator to 6.7 kPa in the tenth-effect evaporator, corresponding to the water saturated temperature from 61.9°C to 38.3°C. Furthermore, the small transfer temperature difference spanning 1.5°C–4°C implies that evaporation capacity is sensitive to the internal pressure drop of HTFFE. Therefore, a good understanding in terms of the configuration of vapor flow resistance in the LT-MED plant is important.

In the one-effect evaporator of the LT-MED plant (usually contains 6–10 effects in total), the shell-side pressure drop (SPD) mainly has four parts along the steam flow path [5,11,12]: (1) Flow resistance of steam flushing the horizontal tube bundle (δp_{tb}); (2) flow resistance of steam passing through the demister (δp_d); (3) flow resistance of steam passing through the axial steam channel (δp_{sc1}); and (4) local resistance of steam flowing out of the steam channel (δp_{sc2}). The tube-side pressure drop (TPD) (δp_c) is the flow resistance inside tubes where steam releases heat and condenses into water along the direction of tube length. These five-part steam flow resistances are important parameters to evaluate the contribution to the reduction in seawater saturated temperature. To date, the composition of SPD has been obtained using experimental measurements or empirical calculations. Liu et al. [13] measured the pressure drop of steam flushing the partial-sized falling film tube bundle and proposed a correlated equation to predict the δp_{tb}. Although the full-sized experiment study can provide reliable test data for designers and researchers, a full-sized tube bundle experiment is expensive and time-consuming to establish because the real evaporator contains tens of thousands of tubes. Other flow resistances (δp_d, δp_{sc}, and δp_c) could be estimated by the velocity-based equations [5]. However, the distribution of flow velocity inside the large-scale evaporator is data shortage in existing literatures which preferred to conduct the vapor/water flow across the single tube [14,15]. For example, Yang et al. [16,17] employed volume of fluid (VOF) method to simulate horizontal-tube falling film evaporation from few tubes and the local velocity and heat transfer coefficients were obtained quite well. In fact, the real case of LT-MED evaporator consists of uncountable tubes which means the velocity distribution at large scale is important for steam flow resistance and needs further investigations.

Under such a circumstance, large-scale numerical simulation may become a possibility to obtain the SPD, TPD, and velocity field in real case of 3D large-scale LT-MED evaporator. However, a large-scale simulation is even impossible to conduct if we consider details of complicated geometric structure and water-vapor two-phase flow in the LT-MED evaporators. To be more specific, if we employ the VOF method to catch the water-vapor flow velocity on over 14,000 falling-film tubes, the computer capacity is overweighed, and numerical results tend to be data divergence. Furthermore, it may get much worse that fluid flow outside the tube bundle region usually interacted with demister and steam channel also solve the VOF-governing equation. Therefore, it is urgent to develop a new and feasible method to solve this existing problem. The porous media (PM) model can be utilized to simplify this physical problem. The PM model has been applied in the computational fluid dynamics (CFD) when involving the multitube bundle arrangement equipment, such as heat exchanger [18] and air-cooled condenser [19]. In this model, the tube bundle region is simplified as PM domain, and pressure losses through the model are considered in the momentum source term. The momentum source term is described from two parts, namely, a viscous coefficient and an inertial resistance coefficient [20]. Accordingly, this method could effectively simplify the geometry and vapor flow process in the shell side and reduce the number of grids as result of less time cost during the numerical computations. Many previous researchers have applied the PM model in the multitube bundle in the engineering field. Sha et al. [21] applied the PM model for the calculation of pressure drop and shell-side flow field in the heat exchangers and obtained favorable results compared with the experimental dataset. Prithiviraj and Andrews [22,23] also utilized this method for the sake of the shell side heat transfer and pressure drop performance in turbulent state. In the air-cooled condenser, the PM model could effectively predict the velocity field and pressure distribution [19,24]. The LT-MED evaporator involves phase change from water to vapor which is in fact a reverse process in condenser. The essence of thermal dynamics in such two heat exchangers are similar. In general, both condenser and evaporator have lots of tubes in an array arrangement where VOF method is impossible to solve so complicated and large-scale governing equations of two-phase flow. Therefore, the PM model becomes an appealing choice to the numerical calculation of flow field, pressure drop, and heat transfer in multitube bundle configuration. It was proven that PM model has been successfully applied for the condenser which means it could also be used in the evaporator.

In the past, the shell-side pressure drop and velocity field distribution in a 3D large-scale LT-MED evaporator have never been systematically reported in CFD simulations because the steam flow interactions with falling seawater is complicated, and the tube number is large. In this study, we applied the PM model in the thermal desalination field for the first time and obtained the compositions of steam flow resistance and velocity/pressure distribution in the full size of first-effect evaporator. Accordingly, the contributions of shell-side and tube-side resistances to the reduction in the saturated heat transfer temperature could be well analyzed. Meanwhile, we also considered the effect of the geometric structure after steam flowed out of the tube bundle and demister. In the PM model simulation, the effect of seawater spray density on the pressure losses was considered into the inertial resistance coefficient. The inertial resistance coefficient was calculated from an additional experiment in which the pressure drop of steam flushing the horizontal tube bundle with falling film was measured. Consequently, the original two-phase (water-vapor) flow could be transferred into a single-phase (vapor) flow in the tube bundle region, which counted on less computer capacity and made the computation easier. Finally, the validity of this model was justified by comparison with the engineering dataset and literature results in real desalination plants. The numerical results in this study could provide a good reference for engineering design optimization and running operation in the field-scale LT-MED plant.

2. Numerical methodology

2.1. Physical model

The main structure of the first-effect evaporator and shell-side steam flow path is systematically shown in Fig. 1. The full-sized evaporator exhibits the shape of a symmetric cylindrical barrel with a diameter of 8,528 mm and an axial length of 11,700 mm. In the vapor flow path, the steam continuously generates from the tube surface (seawater film evaporation) and spontaneously flushes the tube bundle along the two horizontal side direction. The tube bundle region in one symmetric side contains 214 tube rows and 135 tube columns. The tubes are arranged in regular triangular arrays, and each tube diameter and axial length are 25.4 and 6,000 mm, respectively. After the steam reaches the tube bundle outlet, the steam consecutively migrates upward across the four-layer demisters. Each demister is made up of wire meshes with a thickness of 71 mm. When the steam passes through the demister, it enters the axial steam channel in 6,000 mm length and migrates along the axial direction. Finally, the steam flowing out of the axial channel enters a tube-side channel in the next-effect evaporator as the heating resources for evaporation. The steam releases its heat to the water film and condenses into distilled water inside the tubes. It is noted that the whole evaporation and flow process are complicated considering the three-phase interactions of water, vapor, and solid (tube). Establishing a full-sized CFD model is even impossible when considering each geometric detail, especially to the tens of thousands of tube bundle. In this study, some assumptions are used to simplify the physical problems serving the numerical model include the following:

- The tube bundle and demister were simplified as the PM model. The effect of falling water was considered in the resistance coefficients of the PM model. Thus, the two-phase flow could be considered a single-phase of steam flow in the PM.
- The steam generated from the tube surface maintains identical properties, such as density and viscosity, through the whole evaporator.
- No heat transfer occurred between the three phases of water, vapor, and tubes. In this study, we try to find the physical dynamics of steam flow in the evaporator.
- The pressure drop caused by the water droplets in the demister is assumed to be negligible because droplets are assumed to vanish as they hit the demister wires [25].

Base on the above-mentioned assumptions, the complexed two-phase flow is simplified as a single-phase flow problem in the PM. This simplified CFD model allows us to not only obtain good numerical results but also save the computer memories and calculation time, which could be utilized in the large-scale simulation of engineering fields.

2.2. Numerical model

The numerical model was rigorously established according to the real structure of the LT-MED evaporator (Fig. 1) using the commercial software CFD package FLUENT 15.0. Fig. 2 shows the model establishment from the field-scale evaporator. Due to the highly symmetric geometry of evaporator, the half evaporator was selected in the CFD model. As aforementioned, tube bundle and four layers of demisters were regarded as PM domain. The pressure losses and flow characteristics could be described using the properties of PM, such as porosity, viscous coefficient, and inertial resistance coefficient. Other edge surfaces (e.g., seal plates, water tank, and outer wall) were considered the wall boundaries. The steam outlet was the pressure outlet condition. The steam was continuously generated from the position where each tube was arranged using the user defined function (UDF). The overall simulation was working at the operating pressure of 21.8 kPa, corresponding to the vacuum condition in the first-effect evaporator. Turbulence modeling was also employed by the application of the realizable k–ε turbulence model, which has shown substantial improvements over the standard model [26]. The two-phase flow in the evaporator was simplified into a single-phase (water-vapor phase)

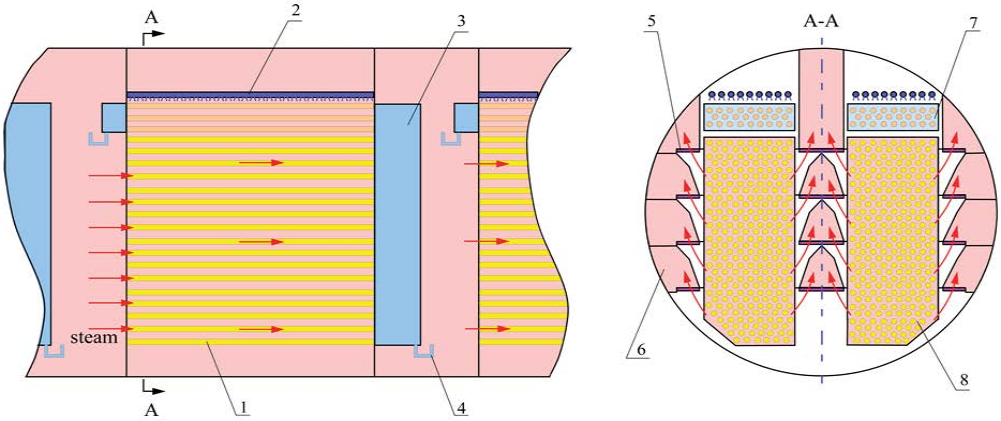

1- Aluminum tube 2- sea water spray system 3- condensate tank 4- condensate pipe
5- wire-mesh demister 6- axial steam channel 7- tube bundle 2 8- tube bundle 1

Fig. 1. The flow path of steam in the LT-MED evaporator.

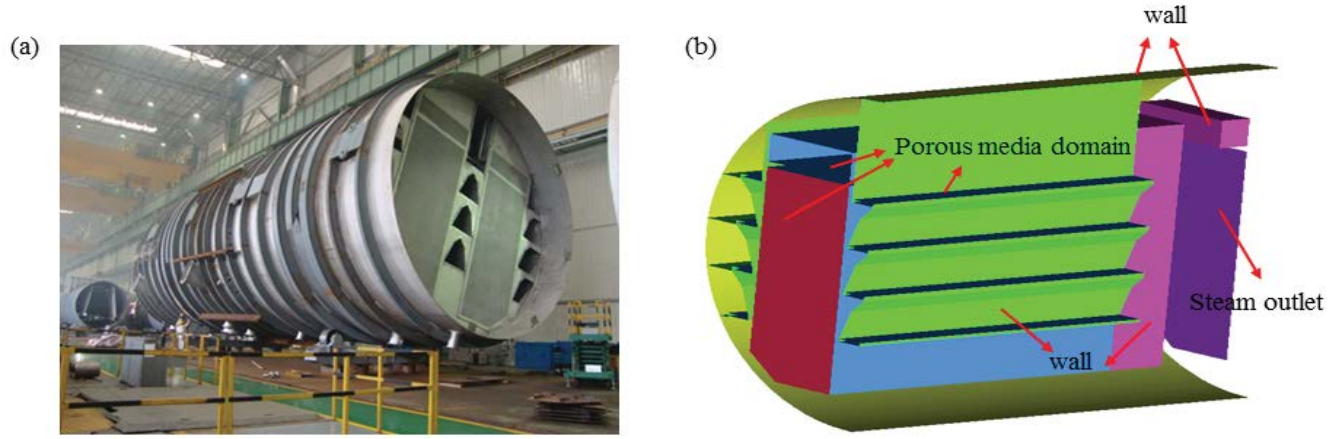

Fig. 2. Establishment of the numerical model: (a) is the photo of a real field-scale evaporator and (b) is modeled using the half-scale of the evaporator due to the high-symmetric geometry. The tube bundle and four-layer demisters are simplified as PM domains.

flow in the LT-MED evaporator. Therefore, the effect of falling water on pressure drop can be considered in the viscous coefficient and inertial resistance coefficient.

2.3. Governing equations

The steam flow in the PM model is generally governed by the mass and momentum transportation [Eqs. (1) and (2)]. By comparison, the PM are modeled by the addition of a momentum source term (S_i) to the standard fluid flow equations. The source term is composed of two parts: a viscous loss and an inertial loss term (Eq. 3) [20].

$$\nabla\cdot\left(\rho\vec{V}\right)=S_m \tag{1}$$

$$\nabla\cdot\left(\rho\vec{V}\vec{V}\right)=-\nabla p+\mu\nabla^2\left(\vec{V}\right)+\rho\vec{g}+S_i \tag{2}$$

where $\vec{V}$ is the superficial velocity based on the volumetric flow rate; ρ and μ are the steam density and dynamic viscosity, respectively; source S_m is the steam mass added in the continuous phase by using the UDF sources; p is the static pressure, and $\rho\vec{g}$ represents the gravitational body force; and S_i denotes the addition of a momentum source term.

$$S_i=-\left(\frac{\mu}{\alpha}\vec{V}+\frac{\rho}{2}C_2\left|\vec{V}\right|\vec{V}\right) \tag{3}$$

where α is the permeability, and C_2 is the inertial resistance coefficient.

The realizable k–ε turbulence model is applied in this numerical simulation. The governing equations for the turbulence kinetic energy (k) and dissipation of turbulence kinetic energy (ε) are as follows:

$$\frac{\partial}{\partial x_j}\left(\rho kV_j\right)=\frac{\partial}{\partial x_j}\left[\left(\mu+\frac{\mu_t}{\sigma_k}\right)\frac{\partial k}{\partial x_j}\right]+G_k+G_b-\rho\varepsilon \tag{4}$$

and

$$\frac{\partial}{\partial x_j}\left(\rho\varepsilon V_j\right)=\frac{\partial}{\partial x_j}\left[\left(\mu+\frac{\mu_t}{\sigma_\varepsilon}\right)\frac{\partial\varepsilon}{\partial x_j}\right]+\frac{C_{1\varepsilon}\varepsilon}{k}\left(G_k+C_{3\varepsilon}G_b\right)-C_{2\varepsilon}\rho\frac{\varepsilon^2}{k} \tag{5}$$

where G_k represents the generation of turbulence kinetic energy due to the mean velocity gradients; G_b is the generation of turbulence kinetic energy due to buoyancy; $C_{1\varepsilon}$ denotes constants; and σ_k and σ_ε are the turbulent Prandtl numbers for k and ε, respectively.

The permeability term could be eliminated in Eq. (3) owing to the modeling of a tube bundle [20], yielding the following simplified form of the momentum source term:

$$S_i=-\left(\frac{\rho}{2}C_2\left|\vec{V}\right|\vec{V}\right) \tag{6}$$

In Eq. (1), the steam mass source term S_m is calculated on the basis of the distillate production in engineering in Section 2.4.4. In Eq. (2), the momentum source term S_i for demister and tube bundle was estimated, respectively, in Sections 2.4.2 and 2.4.3 considering the relationships of steam pressure drop (Δp) and velocity (V).

2.4. Parameter calculation

2.4.1. Porosity of the tube bundle and demister

As previously mentioned, the tube bundle and demister were simplified as the PM models in this study. The porosity of the PM was defined as the ratio of void volume to the total volume, as expressed in Eq. (7).

$$\varphi=\frac{V_{\text{void}}}{V_{\text{total}}} \tag{7}$$

where V_{void} represents the void space of the PM, and V_{total} is the total volume of PM.

According to the engineering data from Fig. 1, the porosity of tube bundle was yielded to be 0.463. In the

engineering field, the porosity of wire-mesh demister is generally 0.9899 [25].

2.4.2. Resistance coefficient of demister

The porous resistance coefficients could be derived from the experimental data of pressure drop against velocity. The relationships between pressure drop and velocity can be plotted to create a trendline yielding the following quadratic equation:

$$\Delta p = AV + BV^2 \tag{8}$$

where A and B are the fitting constant values.

The momentum source term (S_i) and pressure drop (Δp) relationships could be expressed as follows:

$$\Delta p = -\Delta n_i S_i \tag{9}$$

where Δn_i represents the thicknesses of the medium in the coordinate system.

Combining Eqs. (9) and (3) yielded the viscous resistance coefficient ($1/\alpha$) and inertial resistance coefficient (C_2).

$$\frac{1}{\alpha} = \frac{A}{\mu \Delta n_i} \text{ and } C_2 = \frac{2B}{\rho \Delta n_i} \tag{10}$$

Based on the preliminary experimental data of pressure drop as a function of steam velocity through the demister, we yielded Eq. (8) as $\Delta p = 10.84V + 0.061V^2$. Thus, the viscous and inertial resistance coefficients were calculated from Eq. (10) to be 6,629,969 and 5.74, respectively.

2.4.3. Resistance coefficient of tube bundle

As previously mentioned, if the tube bundle is modeled using the PM model, then the viscous resistance coefficient could be ignored, as shown in Eq. (6). From the experimental aspects, the pressure drop of tube bundle against velocity has been summarized by Zhukauskas [27], as shown in Eq. (11).

$$\Delta p = 0.5 f_{\text{sum}} N \rho V^2 \tag{11}$$

where N is the tube column number, and f_{sum} is the coefficient of the total pressure drop when the steam horizontally flushes the tube bundle.

Consequently, combining Eqs. (6), (9) and Eq. (11) yielded the inertial resistance coefficient C_2, as shown in Eq. (12). The key parameter f_{sum} [Eq. (A9)] was obtained on the basis of an additional experiment of measuring the pressure drop as a function of the velocity in the tube bundle with water falling film system. The experimental measuring system is shown in the Appendix section.

$$C_2 = \frac{N \cdot f_{\text{sum}}}{\Delta n_i} \tag{12}$$

In combination with the experimental results [Eqs. (A9) and (12)], the inertial resistance coefficients were calculated to be 99.4 and 26.5 along the X and Y axial direction, respectively, in the numerical model with respect to the rated working condition in engineering.

2.4.4. Mass evaporation rate of vapor

In the PM model, the steam generated from the tube surface was modeled using the UDF codes which has mainly three functions:

- Searching for centerline of each tube where the original tubes are located in the evaporator (tube column × tube row);
- Defining the steam mass source at per tube length and per second (kg/m·s);
- Returning the total mass source rate at per volume (kg/m^3·s).

The UDF codes can assign the steam generation along the real case of tube arrangement, which could reflect real 3D steam flow velocity and pressure distribution. The mass source at per tube length and per second was calculated in average from Eq. (13).

$$\dot{m} = \frac{M}{24 \times 3{,}600 \times \left(L_1 N_1 + L_2 N_2\right)} \tag{13}$$

where M is the freshwater yield in the LT-MED plant; L_1 and N_1 are axial tube length and tube number in the large-effect evaporator, respectively; and L_2 and N_2 are axial tube length and tube number in the small-effect evaporator, respectively. The engineering dataset are listed in Table 1.

The mass source at per tube length and per second (m) is calculated to be 0.2 g/(m·s) in light of Eq. (13) and Table 1. Finally, source term S_m is defined as the total mass flow rate (kg/s) divided by the volume of porous media (m^3) and returns into the Ansys Fluent simulator for stepwise numerical calculation.

2.5. Validation of the PM model

Before starting the simulation work, the PM model in our study must be examined if it could precisely predict the pressure drop of the tube bundle system. To verify the reliability of the PM model, an additional experiment was conducted that the total pressure drop of air flushing the tube bundle with falling water was measured (Appendix). The experimental data were compared with the numerical

Table 1
Engineering design parameters from the 10,000 ton level seawater LT-MED

Name	Value
Freshwater yield (M), kg/d	2.5×10^7
Large effect tube number (N_1)	32,550
Small effect tube number (N_2)	12,454
Large effect tube length (L_1), m	7
Small effect tube length (L_2), m	3

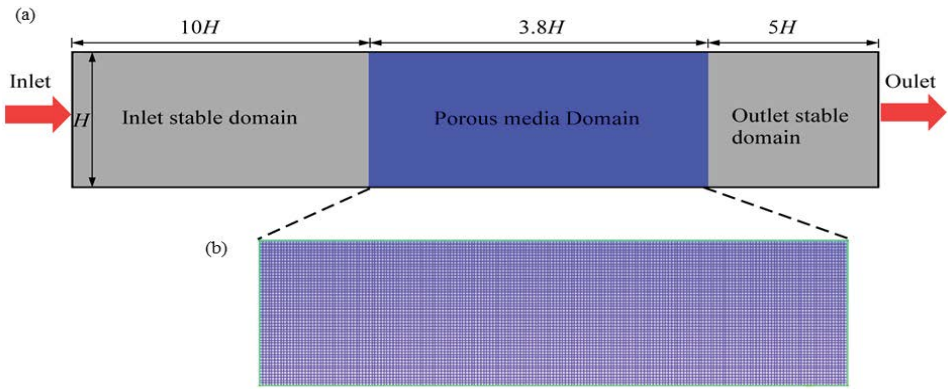

Fig. 3. A numerical model for the experimental tube bundle system. (a) Numerical model and (b) grid system of the PM domain. The blue color is the PM domain that has the same size as the tube bundle system in the additional experiment. Before and after the PM, the inlet and outlet stable regions were arranged.

results obtained by the PM model. The inertial resistance coefficient in the PM model was also calculated using the combined equation of Eqs. (12) and (A9). Accordingly, the two-phase flow was also simplified into single-phase flow in the tube bundle system.

In Fig. 3a, tube bundle was considered the PM domain. The 10*H* distance close to the PM inlet and 5*H* distance close to the PM outlet were arranged to avoid the inlet and outlet effects (*H* = 257.2 mm). The structured grids were generated in the ICEM software (Fig. 3b). The inlet and outlet boundary conditions were the velocity-inlet and pressure-outlet conditions, respectively. The top and bottom layer lines were set as no-slip wall boundary conditions. Similar to the simulation of the 3D full-scale evaporator, the realizable *k*–ε turbulence model was also employed in this justification. This verified simulation was working on the operating condition of the room environment that was as same as the experimental condition.

Fig. 4 shows the comparison of the total pressure drop as a function of the air-inlet velocity at the water spray density of Γ = 0.06 kg/(m s) between the experimental and the numerical results. The numerical results agree well with the experimental results (±1% deviation), thereby indicating that the PM model could precisely predict the pressure drop of tube bundle with a falling water system. Therefore, the PM model is verified reliably in the subsequent numerical simulation of thermal desalination.

2.6. Computational grids and independence verification

Fig. 5a shows the sketch of the 3D grid system, which was meshed based on the 3D numerical model in Fig. 2b. The computational domain was configured with unstructured tetrahedral elements by using the ICEM packages. Before the numerical computation is commenced, the least grid number should be evaluated considering the computational accuracy and time cost. To this end, five cases of grid number, namely, 2017060, 6221410, 9294150, 14787130, and 19229660, were chosen to calculate the velocity of the steam outlet. In Fig. 5b, the velocity reached stability at the grid number of 9294150, beyond which the result was independent on the grid number. Hence, 9294150 was employed as the best grid number for the subsequent numerical computations.

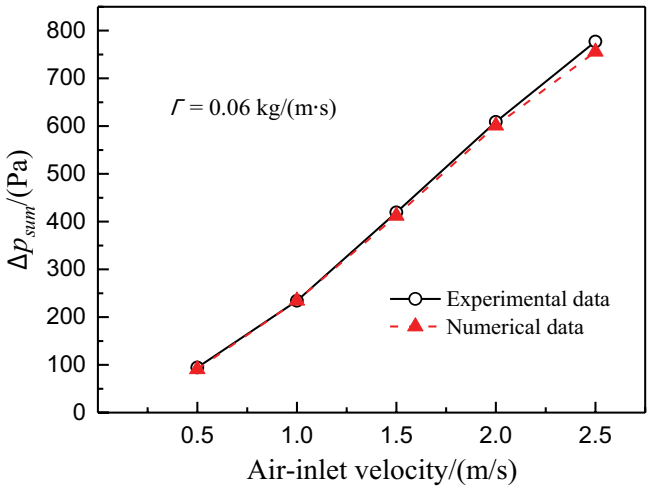

Fig. 4. Comparison of the total pressure drop between the experimental data and the numerical results.

3. Numerical results and discussion

3.1. Justification of the numerical results

In the previous section, the PM model has been justified to be applicable for the numerical simulation of air flushing tube bundle with water falling film system. In this section, the numerical results of the full-sized LT-MED evaporator were again justified through comparison with literature or real LT-MED plants. In this numerical study, the effect of real geometric structure on the steam flow was considered; we maintained the same size and structure as those of the real evaporator after steam flowed out of the tube bundle region. The 3D numerical results have been compared with the previous research, as shown in Table 2. The numerical results in this study show a very good agreement with the previous literature. This notion indicates that the CFD results is accurate enough to predict the steam flow of the thermal evaporator and provide a good reference for engineering design and running simulation. Thereafter, the 3D distribution of velocity field, pressure field, and configuration of resistance are analyzed further as follows:

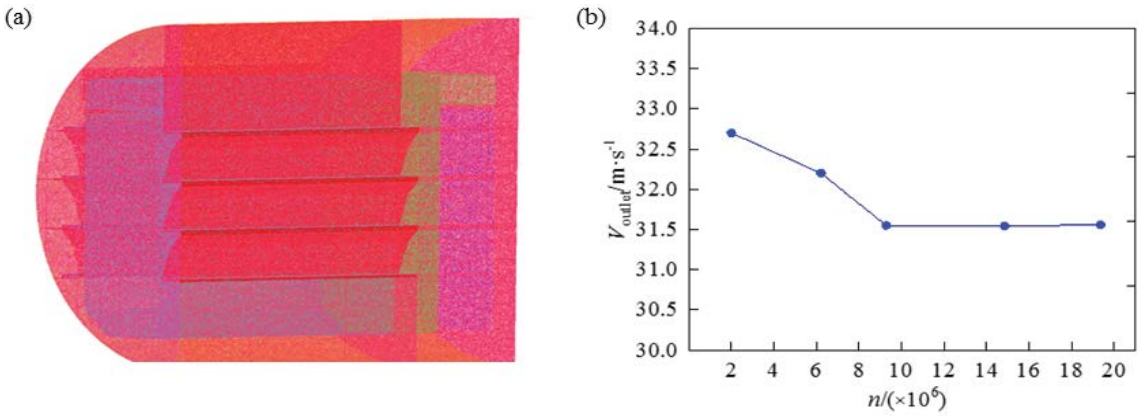

Fig. 5. Grid system and grid independence verification. (a) Sketch of the 3D grid system and (b) steam outlet velocity as a function of grid number.

Table 2
Numerical results vs. literature results

Literature sources	Parameters	Literature values	Current results
Shen et al. [28,29]	Tube-side velocity (m/s)	40–60	53
Gong et al. [30]	Inter-tube velocity (m/s)	0.5–10.5	1–12
Zhou et al. [5]	Total flow resistance (Pa)	347.8	381.6
Zhou et al. [5] and Al-Fulaij et al. [25]	Velocity through demister (m/s)	7, 9	5–13

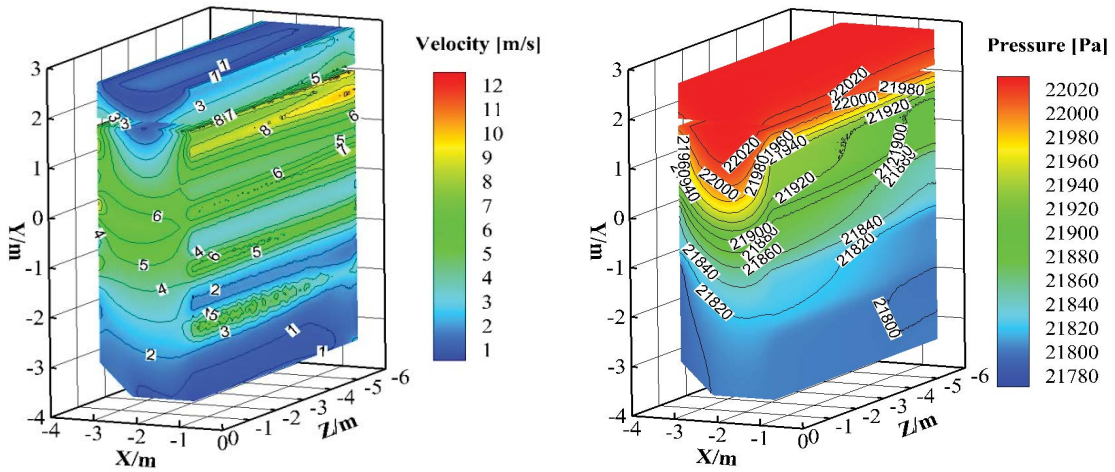

(a) Velocity distribution (b) Pressure distribution

Fig. 6. 3D steam velocity and absolute pressure distribution in the tube bundle region.

3.2. Steam velocity and pressure distribution in 3D pattern

The 3D distribution contour of steam velocity and absolute pressure in the tube bundle domain is shown in Fig. 6a. The steam flows from the middle to the top and bottom layers along the tube row direction at the same time. The steam velocity presents obvious three stratified layers along the tube row direction in the tube bundle region, that is, low velocity at the top layer, high velocity at the middle layer, and low velocity at the bottom layer. At the tube rows of 120–150 (middle layer), the steam velocity reaches the maximum (i.e., 6 m/s). From the middle layer to both sides (top and bottom layers), the steam velocity gradually decreases to 1 m/s. The quantitative velocity as a function of tube rows is more clearly shown in Fig. 7a. The steam velocity variation first increases to the maximum and then decreases with the increasing tube rows. This variation trend is the same as that in Fig. 6a. Therefore, the steam velocity along the vertical direction is characterized as "high value at the middle layer and low

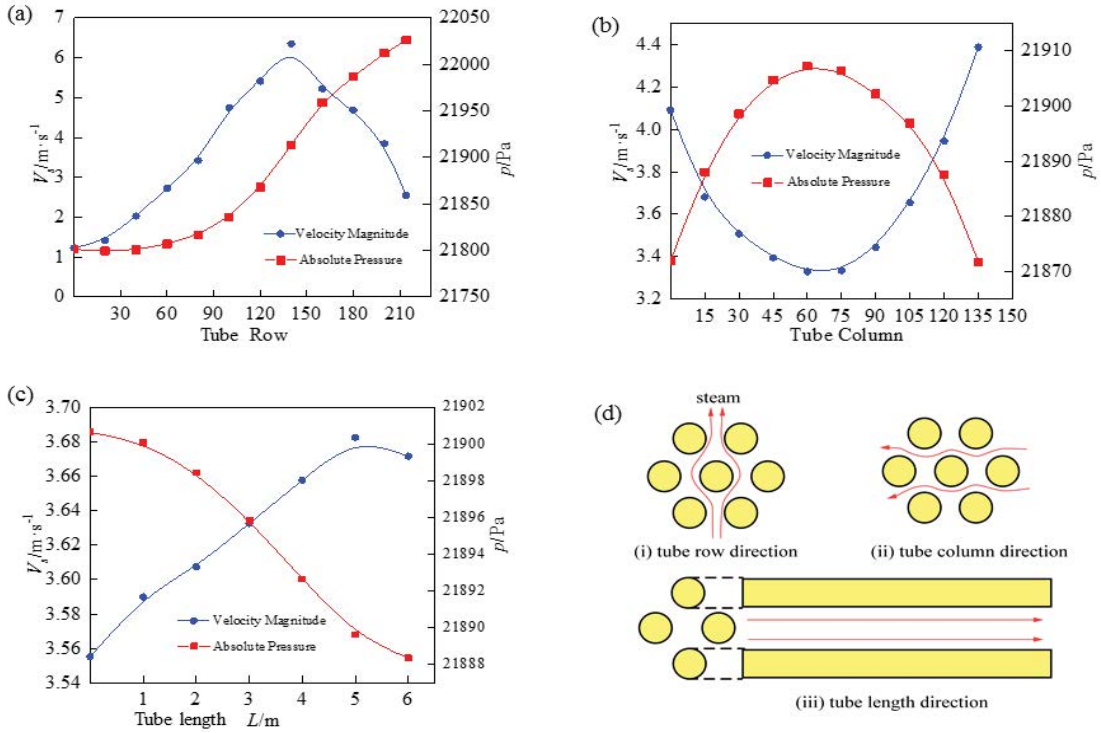

Fig. 7. Quantitative steam velocity and absolute pressure in the tube bundle region. (a–c) represents the velocity and pressure distribution along the tube row, column, and length directions, respectively and (d) is the steam flow path in the real inter-tube system.

value at the top and bottom layers". Such steam velocity field can be attributed to the retention of steam at the top and bottom regions where connectivity to the steam flow channel is unavailable, namely, stagnant region. Along the tube column direction, steam velocity has the lowest value in the middle tube columns, whereas it reaches the highest at both sides of the tube columns (tube bundle outlets) (Fig. 7a). Fig. 7b shows more clearly the quantitative velocity variation as a function of tube columns. The steam velocity shows a highly symmetric parabolic curve owing to the steam that horizontally flushes the tube bundle from the centerline of the tube bundle to both sides. Specifically, the minimum velocity (3.3 m/s) occurs at the tube columns of approximately 60. From the center to one side, the velocity continuously increases to be 4.3 m/s until it flows out of the tube bundle. This phenomenon implies that steam generated from the tube surface gradually accelerates along the horizontal flow direction. The steam also migrates along the tube length direction even though the velocity slightly increases, as shown in Fig. 7c. In Fig. 6a steam velocity close to the axial steam channel is more sensitive when subjected to steam flow in the steam channel where steam continuously accelerates along the tube length direction. This massive acceleration could increase the velocity to a maximum of 50 m/s in axial steam channel, which is large enough to influence the surrounding steam flow. The steam flow path in the tube bundle along the direction of tube rows, columns, and length is presented in Fig. 7d. In the real tube bundle system, the horizontal steam migration is dominant over 80% of the tube bundle region, while the remaining less tube system is dependent on the vertical flow across the tube rows and the axial flow along the tube length direction. This phenomenon occurs because on the one hand, the effective steam flow area along the tube column direction is larger than that along the tube row direction compared with Fig. 7d(i) and (ii), leading to smaller horizontal flow resistance. On the other hand, the axial steam channels are mounted at both sides of tube bundle; therefore, no flow channel exists at the top and bottom tube bundle. The special geometric structure forces the steam flows horizontally. Accordingly, the steam preferentially flushes the tube columns horizontally on the basis of the above-mentioned two aspects. With regard to the steam flowing along the tube-length direction (Fig. 7d(iii)), the closer to the axial channel, the more easily the steam flow is influenced. However, steam in this region will be finally transformed into horizontal flow because it is sealed by the seal plate at the one side and at the end side of tubes.

Fig. 6b shows the 3D pressure distribution in the tube bundle region. In contrast with the velocity distribution, the characteristic of pressure distribution along the vertical direction presents the highest at the top layer, intermediate at the middle layer, and the lowest at the bottom layer. The pressure values along the tube rows are more clearly shown in Fig. 7a. Along the tube row direction from the bottom to the top region, the pressure continuously increases to the highest (i.e., 22,030 Pa). This trend can ascribe to the reason that a portion of steam mass gathers at the top layer because of stagnant flow in this area. In the horizontal direction, the steam pressure curve distributes oppositely compared with that of velocity distribution. Specifically, the lowest velocity corresponds to the highest pressure at

the middle tube columns. Meanwhile, the highest velocity corresponds the lowest pressure at the two outlets of the tube columns. Theoretically, this variation of velocity and pressure trend is aligned well with Bernoulli's Law [31]. Along the tube length direction, the pressure constantly decreases also in agreement with Bernoulli's Law, according to the constant increase in the steam velocity.

In the following, the velocity and pressure distribution in the axial steam channel are presented and analyzed. In Fig. 8, cross-sectional regions in the steam channel are marked with F_1 and F_2 surfaces, which are the representatives of the left-side and right-side steam channels, respectively. In the right-side surface F_1, the steam channel is marked with Arabic numerals 1–4. In the left-side surface F_2, the steam channel is marked with 5–8. The length of the axial steam channel approaches 6 m until the outlet. After the outlet of steam channel, a vast volumetric space is linked with the steam outlet, which connects to the next-effect tube-side channels.

Fig. 9 shows the distribution of steam velocity and pressure iso-contours in the region of the cross-sectional steam channel. The steam velocity in the steam channel is up to one order of magnitude larger than that in the tube bundle system compared with the tube bundle region (Fig. 9a and c). This phenomenon shows that the steam channels collect the overall steam mass generated from the tube bundle system, resulting in the large increase in steam velocity. Furthermore, a typical characteristic in each channel presents that velocity gradually increases from 5 m/s to the maximum 50 m/s. This giant variation originates from the reason that the massive steam volume is forced to form a steam jet to the outlet. After the steam flows out of each steam channel, all the steam starts to enter a vast space and mixed with each other, thereby leading to a large decrease in velocity. In addition, the steam velocity in each layer of the channel varies from the height located in the position. The steam velocity also increases with increasing vertical height, which is possibly associated with the vertical steam migration direction (tube row direction), as mentioned in Figs. 6a and 7a. Fig. 9a and c demonstrate that the steam velocity in the demisters is up to approximately 5–13 m/s, which is the same order of magnitude as that in the tube bundle region.

Fig. 9b and d present the pressure distribution contours in the cross-section steam channel. The steam pressure constantly decreases when the steam flows along the axial length. After steam jets into each channel outlet, the pressure decreases to the minimum (i.e., 21,580 Pa). The steam velocity corresponds to the pressure very well according to Bernoulli's Law.

Fig. 10 shows the quantitatively extracted volume-average steam velocity distribution in each steam channel. The velocity in each axial steam channel of 1–8 gradually increases up to the maximum, approaching 35 m/s, as a function of tube length. When the steam jets into the outlet, the steam velocity drastically decreases due to the entrance to the larger space. The drastic velocity changes during and after the axial channels imply that a large local steam flow resistance could be induced, which could have a great influence on the reduction of saturated water temperature. The velocity in the steam channel varies from its height location, namely, velocity rises with increasing height position, which is consistent with the velocity contours in Fig. 9. We also observed that the velocity in left-side channels 5–8 is larger than that in the right-side channel, except channel 4. This result is closely related to the channel size (flow volume). For instance, channel 4 shows a steam velocity much larger than the others because the flow volume in channel 4 is 2.4 times than others. Therefore, channel 4 could accommodate more steam mass than others as result of larger velocity.

3.3. Configurations of flow resistance and thermodynamic losses

Fig. 11 shows the various steam flow resistance and corresponding saturated temperature depression in the first-effect evaporator of the LT-MED plant. In Fig. 11a, the total flow resistance components consist of tube bundle, demister, and axial steam channel resistances of the

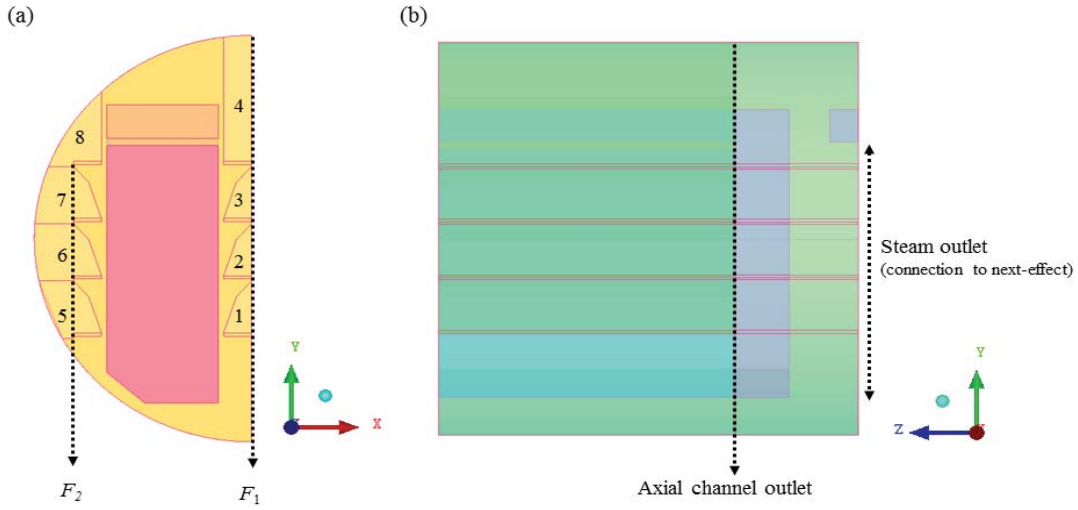

Fig. 8. Axial channel in the cross-sectional region. F_1 is the right-side steam channel marked with numbers 1–4, and F_2 is the left-side steam channel marked with numbers 5–8.

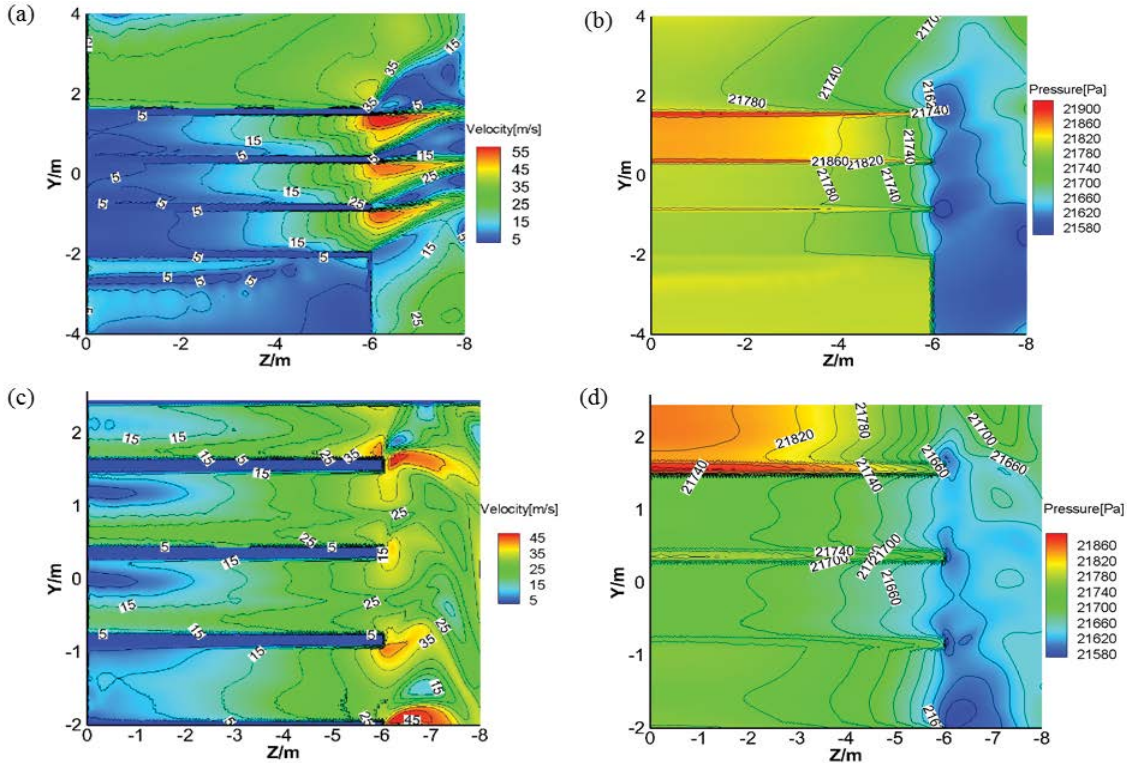

Fig. 9. Steam velocity and absolute pressure contours in the axial steam channel. (a)–(b) are the contours in the surface of F_1, and (c)–(d) are the contours in the surface of F_2.

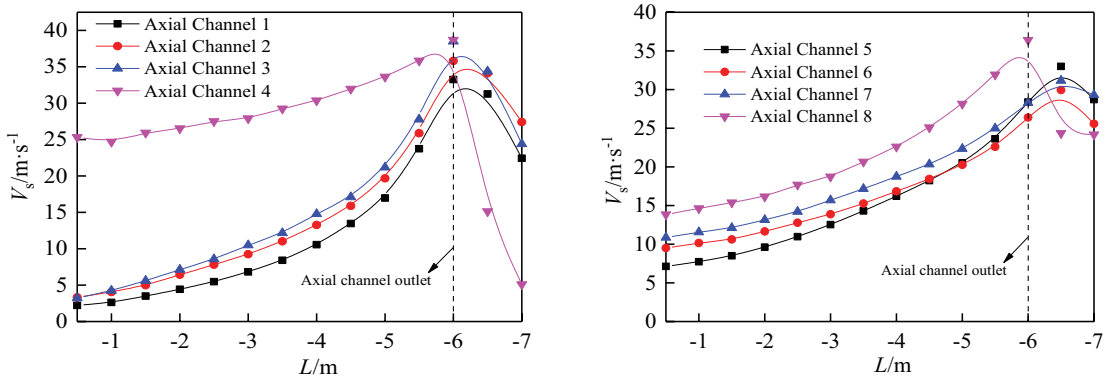

(a) Axial channel 1–4 (b) Axial channel 5–8

Fig. 10. 3D average velocity distribution in the axial steam channel along the axial direction.

shell-side and condensation process resistance of the tube-side, which occupy a total flow resistance of 381.6 Pa. In the shell-side flow resistance, the steam channel resistance produces 220 Pa, accounting for the largest proportion (57.6%) of total flow resistance. Tube bundle and demister resistance contribute a similar magnitude to the total flow resistance with values of 39.5 and 32.1 Pa, respectively, which correspond to the previous research results [5]. The proportions of these two parts to total resistance are up to 10.4% and 8.4%, respectively. The tube-side resistance is estimated on the basis of our steam-inlet velocity inside the tube referred to Shen et al.'s [29] experimental research. In our study, the numerical steam-outlet velocity of connection to the next-effect evaporator is 31.5 m/s. Accordingly, the tube-side inlet velocity is calculated to be 53 m/s in average. Therefore, the tube-side condensation resistance is concluded to be 90 Pa, contributing 23.6% proportion to the total flow resistance. Fig. 11b presents the saturated temperature depression by the above-mentioned steam flow resistances. This figure shows that the total flow resistance results in 0.38°C of saturated temperature depression in total wherein tube bundle, demister, steam channel, and condensation process contribute 0.04°C, 0.03°C, 0.22°C, and 0.09°C to the reduction in saturated temperature,

respectively. Obviously, the largest contribution to the temperature depression is the shell-side vapor flow resistance, accounting for 0.29°C, which indicates the steam flow resistance has great effect on the thermal evaporation.

The effective heat transfer temperature difference ($\Delta T_{effective}$) is the apparent heat transfer temperature difference ($\Delta T_{apparent}$) apart from the boiling point elevation (BPE) and saturated temperature depression (δT_p) caused by the above-mentioned steam flow resistances. $\Delta T_{effective}$ is defined as the real heat transfer temperature difference between the in-side (heating steam) and out-side tubes (sea water), which is given in Eq. (14) [5]:

$$\Delta T_{effective} = \Delta T_{apparent} - BPE - \delta T_p \quad (14)$$

where $\Delta T_{apparent}$ = 3.1°C, BPE = 0.7°C, and δT_p = 0.38°C in this study. In this first-effect evaporator, the tube-side heating steam temperature is 65°C, and the designed saturated water temperature is 61.9°C. Therefore, the apparent heat transfer temperature difference should be 3.1°C. BPE is also a necessary component that compensates for thermal losses. However, this notion is not the main point studied in this study. The BPE value is obtained from the reference (i.e., 0.7°C) [5]. The saturated temperature depression caused by the flow resistance has been analyzed as mentioned above (i.e., 0.38°C).

The proportions of various thermodynamic losses and effective heat transfer temperature difference are shown in Fig. 12. The effective heat transfer temperature difference accounts for only 65.2% of the total apparent heat transfer temperature difference due to the BPE loss (22.6%) and temperature depression (12.2%). Therefore, the steam flow resistance has a great reduction in the effective heat transfer temperature difference. As previously mentioned, the total steam flow resistance is summarized as 381.6 Pa, which is a very small magnitude compared with the other tube bundle systems, such as heat exchanger. In addition, the apparent heat transfer temperature difference is only within 1.5°C–4°C. Accordingly, the small flow resistance has a significant influence on the reduction in the small heat transfer temperature difference. This phenomenon is characterized as "low resistance, high influence" in the LT-MED evaporator and prevails in all vacuum thermal desalination plant with a horizontal tube bundle system. This study also reveals that the largest flow resistance produces in the steam channel, thereby providing a good reference for resistance optimization in engineering.

4. Conclusions

This study numerically calculated the 3D steam flow velocity and flow resistance distributions in the first-effect

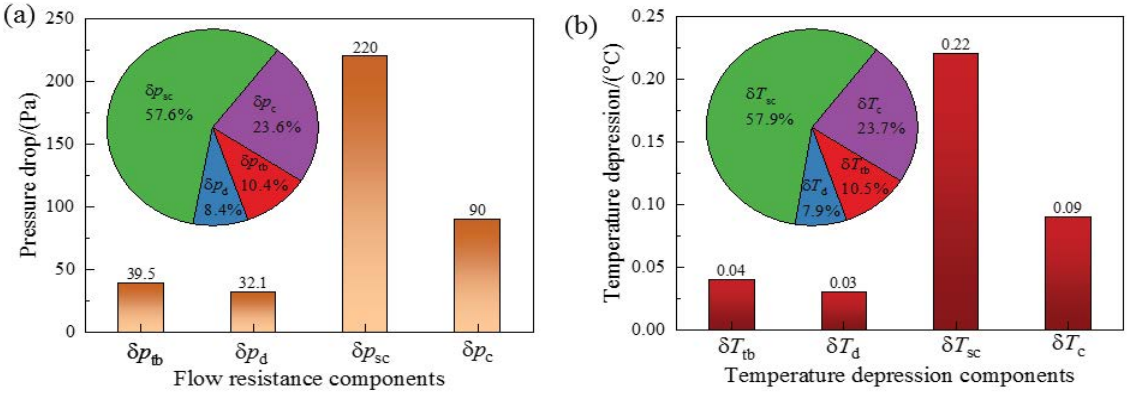

Fig. 11. Components of (a) steam flow resistance and (b) saturated temperature depression in the first-effect evaporator in the LT-MED system. The inset of (a) is the proportion that accounts for the total flow resistance; the inset of (b) is the proportion that accounts for the total saturated temperature depression by the flow resistance.

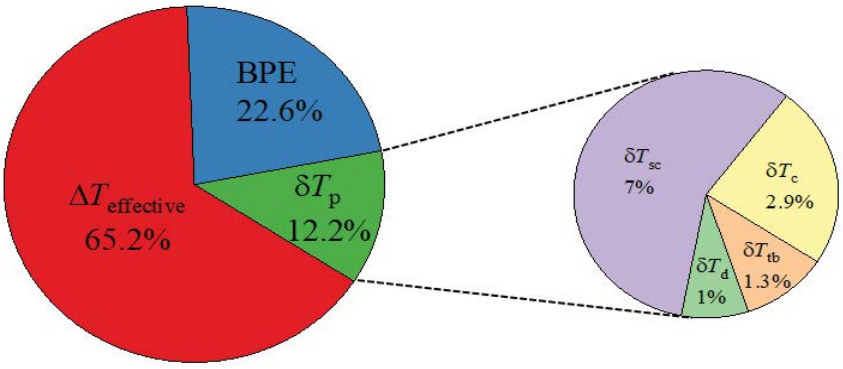

Fig. 12. Proportions of thermodynamic losses in the first-effect evaporator in the LT-MED system.

LT-MED plant by using the simplified PM model. The resistance coefficient in PM model was obtained from an additional experiment that measured the pressure drop of steam flushing the tube bundle with falling water. The PM model was proven to be applicable for predicting the pressure drop in the tube bundle system. The 3D numerical results were believable compared with the engineering dataset in real plants. The following main conclusions in this study can be suggested:

- The PM model is potential for simulating the steam flow process in the LT-MED plant with a horizontal tube bundle system. The two-phase flow could be simplified as a single-phase flow in the tube bundle region, which enables the complicated numerical simulation to become feasible.
- The steam velocity distributes in the tube bundle region with a value ranging from 1 to 12 m/s. Along the direction of the tube column, the velocity constantly increases from the tube bundle centerline to both sides' outlet due to the steam accumulation. Along the direction of the tube row, the velocity reaches the maximum 6 m/s at the row number of 120–150. From the center to the top and bottom rows, the velocity greatly decreases. The velocity variation along the tube-length direction continues to increase when subjected to the steam flow in the axial steam channel. The steam pressure distribution presents three stratified layers, that is, maximum at the top, intermediate at the center, and minimum at the bottom regions.
- The steam velocity greatly increases up to the maximum of 55 m/s in the axial steam channel. After flowing out of the outlet, the velocity considerably decreases. The pressure variation presents the opposite change compared with the velocity.
- The steam flow resistance components include the tube bundle, demister, steam channel, and condensation resistances, which correspond to the proportions of 10.4%, 8.4%, 57.6%, and 23.6% of the total flow resistance, respectively. The flow resistance in the steam channel contributes the largest reduction to the saturated temperature depression, which should be paid great attention in the future plant design.
- The contribution of steam flow resistance to the thermodynamic losses is up to 12.2%. The small flow resistance of 381.6 Pa results in a conspicuous decrease in the apparent heat transfer temperature difference, especially at the vacuum operating condition with a tiny temperature difference of 1.5°C–4°C. This characteristic of "low resistance, high influence" prevails in all vacuum thermal desalination plants with a horizontal tube bundle system.

Declaration of competing interest

The authors declare that they have no known competing financial interests or personal relationships that could have appeared to influence the work reported in this paper.

Acknowledgements

This work was supported by Shenhua Guohua (Beijing) Electric Power Research Institute Co., Ltd. Project No. 20161048 recorded in Xi'an Jiaotong University.

References

[1] J. Alcamo, P. Döll, F. Kaspar, S. Siebert, Global Change and Global Scenarios of Water Use and Availability: an Application of WaterGAP 1.0., University of Kassel, Kassel, Germany, 1997.
[2] R.K. Chakraborti, J. Kaur, H. Kaur, Water shortage challenges and a way forward in India, J. Am. Water Works Assn., 111 (2019) 42–49.
[3] A. Subramani, J.G. Jacangelo, Emerging desalination technologies for water treatment: a critical review, Water Res., 75 (2015) 164–187.
[4] A.D. Khawaji, I.K. Kutubkhanah, J.M. Wie, Advances in seawater desalination technologies, Desalination, 221 (2008) 47–69.
[5] S. Zhou, Y. Guo, X. Mu, S. Shen, Effect of design parameters on thermodynamic losses of the heat transfer process in LT-MEE desalination plant, Desalination, 375 (2015) 40–47.
[6] L. Gong, S. Shen, H. Liu, X. Mu, X. Chen, Three-dimensional heat transfer coefficient distributions in a large horizontal-tube falling film evaporator, Desalination, 357 (2015) 104–116.
[7] A. Ophir, F. Lokiec, Advanced MED process for most economical sea water desalination, Desalination, 182 (2005) 187–198.
[8] Y. Xue, X. Du, Z. Ge, L. Yang, Study on multi-effect distillation of seawater with low-grade heat utilization of thermal power generating unit, Appl. Therm. Eng., 141 (2018) 589–599.
[9] A. Rezaei, A. Naserbeagi, G. Alahyarizadeh, M. Aghaei, Economic evaluation of Qeshm island MED-desalination plant coupling with different energy sources including fossils and nuclear power plants, Desalination, 422 (2017) 101–112.
[10] J. Leblanc, J. Andrews, Low-Temperature Multi-Effect Evaporation Desalination Systems Coupled with Salinity-Gradient Solar Ponds, Proceedings of ISES World Congress 2007, Springer, Berlin, Heidelberg, 2007, pp. 2151–2157.
[11] H.T. El-Dessouky, H.M. Ettouney, F. Mandani, Performance of parallel feed multiple effect evaporation system for seawater desalination, Appl. Therm. Eng., 20 (2000) 1679–1706.
[12] S. Zhou, L. Gong, X. Liu, S. Shen, Mathematical modeling and performance analysis for multi-effect evaporation/multi-effect evaporation with thermal vapor compression desalination system, Appl. Therm. Eng., 159 (2019) 113759, doi: 10.1016/j.applthermaleng.2019.113759.
[13] H. Liu, S.Q. Shen, L.Y. Gong, S. Chen, Shell-side two-phase pressure drop and evaporation temperature drop on falling film evaporation in a rotated square bundle, Appl. Therm. Eng., 69 (2014) 214–220.
[14] F. Tahir, A. Mabrouk, M. Koç, Influence of co-current vapor flow on falling film over horizontal tube, Int. J. Therm. Sci., 159 (2021) 106614, doi: 10.1016/j.ijthermalsci.2020.106614.
[15] F. Tahir, A. Mabrouk, M. Koç, Impact of surface tension and viscosity on falling film thickness in multi-effect desalination (MED) horizontal tube evaporator, Int. J. Therm. Sci., 150 (2020) 106235, doi: 10.1016/j.ijthermalsci.2019.106235.
[16] L. Yang, Y. Liu, Y. Yang, S. Shen, Microscopic mechanisms of heat transfer in horizontal-tube falling film evaporation, Desalination, 394 (2016) 64–71, doi: 10.1016/j.desal.2016.04.014.
[17] L. Yang, Z. Xu, X. Zhang, S. Shen, Characterization of the microscopic mechanics in falling film evaporation outside a horizontal tube, Desal. Water Treat., 55 (2015) 3330–3335.
[18] M. Prithiviraj, M.J. Andrews, Comparison of a three-dimensional numerical model with existing methods for prediction of flow in shell-and-tube heat exchangers, Heat Transfer Eng., 20 (1999) 15–19.
[19] X. Gao, C. Zhang, J. Wei, B. Yu, Numerical simulation of heat transfer performance of an air-cooled steam condenser in a thermal power plant, Heat Transfer Eng., 45 (2009) 1423–1433.
[20] F. Ansys, ANSYS Fluent Theory Guide, ANSYS Inc., USA, 2013, pp. 724–746. Available at: http://www.afs.enea.it/project/neptunius/docs/fluent/html/th/main_pre.htm
[21] W.T. Sha, C.I. Yang, T.T. Kao, S.M. Cho, Multidimensional numerical modeling of heat exchangers, J. Heat Transfer, 104 (1982) 417–425.
[22] M. Prithiviraj, M.J. Andrews, Three dimensional numerical simulation of shell-and-tube heat exchangers. Part I: foundation

and fluid mechanics, Numer. Heat Transfer, Part A, 33 (1998) 799–816.
[23] M. Prithiviraj, M.J. Andrews, Three-dimensional numerical simulation of shell-and-tube heat exchangers. Part II: Heat transfer, Numer. Heat Transfer, Part A, 33 (1998) 817–828.
[24] Y. Zhou, Y.L. Cheng, N. Zhang, H.B. Shi, Numerical simulation study of novel air-cooled condenser with lateral air supply, Case Stud. Therm. Eng., 13 (2019) 100354, doi: 10.1016/j.csite.2018.11.005.
[25] H. Al-Fulaij, A. Cipollina, G. Micale, H. Ettouney, D. Bogle, Eulerian-lagrangian modeling and computational fluid dynamics simulation of wire mesh demisters in MSF plants, Desalination, 385 (2016) 148–157.
[26] T.-H. Shih, W.W. Liou, A. Shabbir, Z. Yang, J. Zhu, A new k-ϵ eddy viscosity model for high reynolds number turbulent flows, Comput. Fluids, 24 (1995) 227–238.
[27] A.A. Zhukauskas, Convective Transfer in Heat Exchangers, Science Press, Moscow, 1982.
[28] S. Shen, L. Gong, H. Liu, X. Mu, R. Liu, Characteristic study of steam maldistribution in horizontal-tube falling film evaporators, Appl. Therm. Eng., 75 (2015) 635–647.
[29] S. Shen, R. Liu, Y. Yang, X. Liu, J. Chen, Condensation character of a stratified flow inside a horizontal tube, Desal. Water Treat., 33 (2011) 218–223.
[30] L. Gong, S. Shen, H. Liu, X. Mu, Parametric distributions of a horizontal-tube falling film evaporator for desalination, Desal. Water Treat., 57 (2016) 11699–11711.
[31] C. Schär, A generalization of Bernoulli's theorem, J. Atmos. Sci., 50 (1993) 1437–1443.
[32] Y. She, W. Chan, F. Chang, K. Guo, Y. Zhang, H. Li, Experimental investigation on the characteristics of pressure drop and air/vapor flow over horizontal tube bundle with water-spray falling film, Desal. Water Treat., 216 (2021) 34–46.
[33] H. Blasius, Das aehnlichkeitsgesetz bei reibungsvorgängen in flüssigkeiten, Mitteilungen Über Forschungsarbeiten Auf Dem Gebiete Des Ingenieurwesens, Springer, Berlin, Heidelberg, 1913, pp. 1–41.
[34] R.W. Lockhart, R.C. Martinelli, Proposed correlation of data for isothermal two-phase two component flow in pipes, Chem. Eng. Prog., 45 (1949) 39–48.

Appendix A: Additional experiment

A1. Experimental setup

To obtain f_{sum}, an extra experimental system that air flushed the horizontal tube bundle with falling water was conducted, as shown in Fig. A1a. In this system, the steam was replaced with air to mimic the steam flow process in the tube bundle. The steam–air velocity relationship was tabulated in Table A1 by using the similarity principle. In this study, the tube bundle was arranged in a regular triangle style (Fig. A1c), which contains 10 rows and 60 columns with a total tube number of 300. The tube bundle region selected in our system was just a local-sized area in the first-effect evaporator where the steam flushing direction was similar to that in our experiment. The pressure drop between the inlet and the outlet of the tube bundle was measured with a Rosemount differential pressure sensor with a measuring range of 0–2,480 Pa. The pressure drop measurement system was clearly shown in Fig. A1b. Refer to our previous research [32] for details of this experiment and analysis.

The experimental procedures are as follows:

- Open the water pump to create steady water falling from the top tube to the bottom tube. The water flow rate was controlled by the flowmeter, which was used for the calculation of water spray density (Γ) ranging from 0 to 0.10 kg/(m s) (interval: 0.02 kg/(m s)).
- Switch on the centrifugal fan to provide the air velocity of 0.5–2.5 m/s to cross the falling film tube bundle (interval: 0.5 m/s). The air velocity was precisely controlled with the airflow meter.
- The pressure drops were recorded because the air flushing and water flow were monitored to be in dynamic equilibrium (pressure drop reading became stable).

A2. Pressure drop correlation

The pressure drop correlation was proposed after the data acquisition of the pressure drop as a function of different air velocities and spray densities. The special falling-film crossflow was different from that of the traditional two-phase flow in the tube bundle. Specifically, special falling-film crossflow means that air flushes the tube bundle with falling water along the gravitational direction, while the traditional two-phase flow is the mixture of air and water crossing the tube bundle along the same direction. Considering the specialty and complexity of the two-phase flow in the tube bundle in low-temperature multi-effect desalination, a brand-new correlation should be comprehensively proposed, which is directly used for f_{sum} calculation. To this end, the total pressure drop (Δp_{sum}) was divided into two individual parts, as shown in Eq. (A1), namely, the pressure drop of the airflow flushes the tube bundle without spray water (Δp_{tb}) and that of airflow flushes the liquid columns (Δp_{col}). The former was proposed on the basis of the Blasius-type formula [33], while the latter was based on the dimensionless analytical method. In this manner, the influencing factor on the interactions of air and liquid phases can be comprehensively and reasonably analyzed.

$$\Delta p_{sum} = \Delta p_{tb} + \Delta p_{col} = 0.5N\rho_g f_{sum} V_{inlet}^2 \tag{A1}$$

where N is the tube column number, f_{sum} is the coefficient of the total pressure drop when air horizontally flushes the tube bundle, and V_{inlet} denotes the air-inlet velocity in the tube bundle.

- Tube bundle pressure drop (Δp_{tb})

The pressure drop of air flushing the horizontal tube bundle without spray water is expressed as Eq. (A2).

$$\Delta p_{tb} = 0.5N\rho_g f_{tb} V_1^2 \tag{A2}$$

where f_{tb} is the coefficient of pressure drop when air horizontally flushes the tube bundle without water spray, which is usually proposed as Eq. (A3); V_1 denotes the actual inter-tube air velocity in the non-spray tube bundle, and the

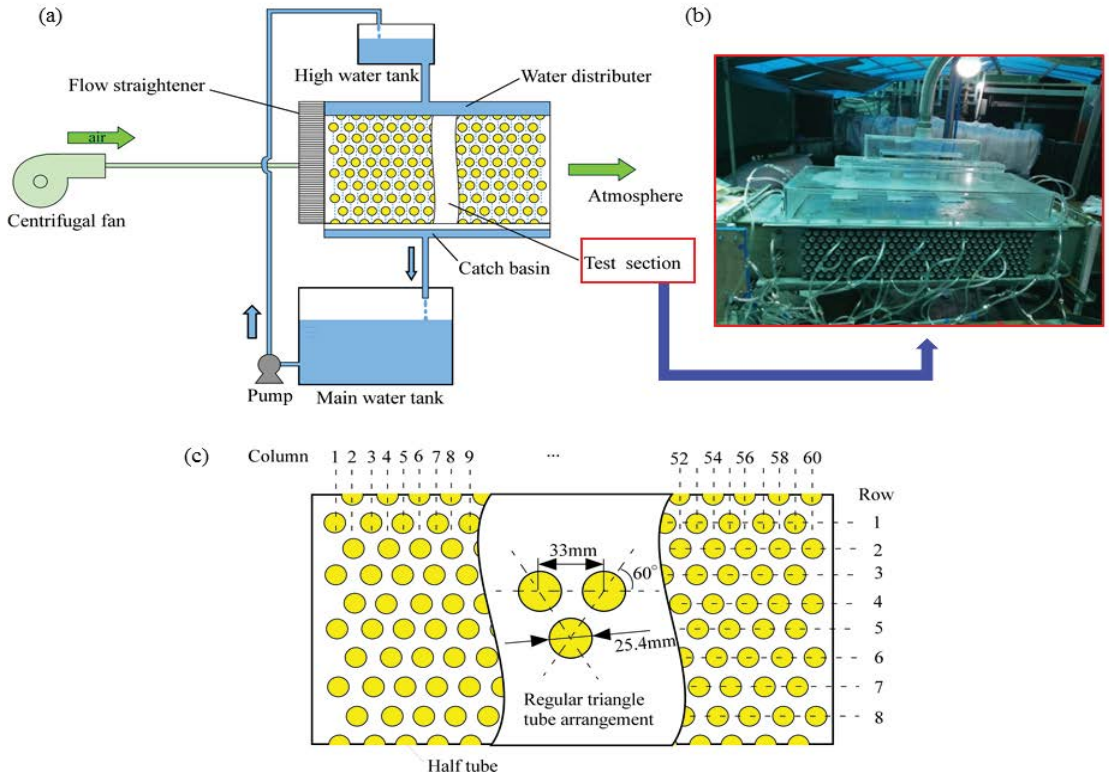

Fig. A1. Experimental system and test section. (a) Diagram of the experimental system, (b) photography of the test section, and (c) arrangement of the regular triangular tube bundle.

Table A1
Air–vapor velocity relationship in the experiment system

Air-inlet velocity (m/s)	Steam-inlet velocity (m/s)
0.5	2.6
1.0	5.3
1.5	7.9
2	10.6
2.5	13.2

relationship of V_1 and V_{inlet} could be yielded V_1 = 1.8 V_{inlet} in our experiment.

$$f_{tb} = A\,\mathrm{Re}_1^B \tag{A3}$$

where Re_1 is the Reynolds number based on V_1, and A and B are constants.

- Liquid column pressure drop (Δp_{col})

The liquid was assumed as a cylindrical liquid column with an equal average diameter of d = 2.3 mm. Consequently, the air that flushes the liquid columns could be described as Eq. (A4).

$$\Delta p_{tb} = 0.5N\rho_g C_d V_{2^*}^2 \tag{A4}$$

where C_d is the pressure drop coefficient of the circular cylinders, and V_{2^*} denotes the corrected inter-tube air velocity in the water-spray tube bundle considering the interactions of the two-phase flow using the dimensionless analytical method.

The corrected air velocity V_{2^*} has been influenced by many factors, such as turbulence between the two phases, fluid physical properties, and Reynolds number. The formula could be described as Eq. (A5).

$$V_{2^*} = f\left(V_2, V_l, \rho_g, \rho_l, \mu_g, \mu_l, g, d, D, 1-x/x\right) \tag{A5}$$

where V_2 is the ideal inter-tube velocity in the tube bundle with a water-spray density, and relationship of V_2 and V_{inlet} could be yielded as V_1 = 2.034 V_{inlet} in our experiment; V_l is the water-spray velocity out of the spray orifices; ρ_g and ρ_l are air density and water density, respectively; μ_g and μ_l are air dynamic viscosity and water dynamic viscosity, respectively; g denotes the gravitational acceleration; d and D represent the liquid column diameter and tube outer diameter, respectively; and x is the air fraction inside the tube bundle.

Subsequently, Eq. (A5) is formed as dimensionless-controlled variations, as shown in Eq. (A6):

$$\frac{V_{2^*}}{V_2} = f\left(\mathrm{Fr}_g, \frac{\mathrm{Re}_l}{\mathrm{Re}_2}, X_{tt}\right) \tag{A6}$$

where Fr_g is the Froude number, Re_l is the water-spray Reynolds number, Re_2 is the air Reynolds number based on V_2, and X_{tt} is the Lockhart–Martinelli number [34].

Accordingly, Eq. (A6) can be further expressed as follows:

$$\frac{V_{2^*}}{V_2} = a_0 + X_{tt}^{a_1} \cdot \left(\frac{Re_l}{Re_2}\right)^{a_2} \cdot Fr^{a_3} \tag{A7}$$

Therefore, the coefficient of liquid column pressure drop (f_{col}) could be described as follows:

$$f_{col} = C_d \left[a_0 + X_{tt}^{a_1} \cdot \left(\frac{Re_l}{Re_2}\right)^{a_2} \cdot Fr^{a_3} \right]^2 \tag{A8}$$

- Total pressure drop coefficient (f_{sum})

According to the total pressure drop equation description [Eq. (A1)], the coefficient of total pressure drop f_{sum} could be yielded as Eq. (A9) in combination with Eqs. (A2)–(A4), and (A8).

$$f_{sum} = 3.24 A Re_1^B + 4.14 C_d \left[a_0 + X_{tt}^{a_1} \cdot \left(\frac{Re_l}{Re_2}\right)^{a_2} \cdot Fr^{a_3} \right]^2 \tag{A9}$$

where a_0, a_1, a_2, and a_3 are correlated constants, and the values are −1.44, 0.386, −0.336, and 0.00522 in this experiment, respectively; the constants of A and B are 12.8 and −0.46, respectively. These variables were obtained using the least square multiple regression to fit the experimental data.